RSC Advances

PAPER

View Article Online
View Journal | View Issue

Cite this: *RSC Adv.*, 2024, **14**, 5440

Bandgap reduction and efficiency enhancement in $Cs_2AgBiBr_6$ double perovskite solar cells through gallium substitution

Ihtisham-ul-haq,[a] M. I. Khan, *[a] Asad Ullah,[a] Ali Mujtaba, [a] Badriah S. Almutairi, [b] Wajeehah Shahid,[a] Asghar Ali[a] and Jeong Ryeol Choi*[c]

Lead-free halide double perovskite (LFHDP) $Cs_2AgBiBr_6$ has emerged as a promising alternative to traditional lead-based perovskites (LBPs), offering notable advantages in terms of chemical stability and non-toxicity. However, the efficiency of $Cs_2AgBiBr_6$ solar cells faces challenges due to their wide bandgap (E_g). As a viable strategy to settle this problem, we consider optimization of the optical and photovoltaic properties of $Cs_2AgBiBr_6$ by Gallium (Ga) substitution. The synthesized $Cs_2Ag_{0.95}Ga_{0.05}BiBr_6$ is rigorously characterized by means of X-ray diffraction (XRD), UV-vis spectroscopy, and solar simulator measurements. XRD analysis reveals shifts in peak positions, indicating changes in the crystal lattice due to Ga substitution. The optical analysis demonstrates a reduction in the E_g, leading to improvement of the light absorption within the visible spectrum. Importantly, the $Cs_2Ag_{0.95}Ga_{0.05}BiBr_6$ solar cell exhibits enhanced performance, as evidenced by higher values of open circuit voltage (V_{oc}), short-circuit current (J_{sc}), and fill factor (FF), which are 0.94 V, 6.01 mA cm^{-2}, and 0.80, respectively: this results in an increased power conversion efficiency (PCE) from 3.51% to 4.52%. This research not only helps to overcome film formation challenges, but also enables stable $Cs_2Ag_{0.95}Ga_{0.05}BiBr_6$ to be established as a high-performance material for photovoltaic applications. Overall, our development contributes to the advancement of environmentally friendly solar technologies.

Received 31st December 2023
Accepted 30th January 2024

DOI: 10.1039/d3ra08965g

rsc.li/rsc-advances

1. Introduction

As a sustainable energy resource, solar energy emerges as a distinctive solution to cope with the global energy crisis and environmental pollution that accompanies the use of traditional energy. Consequently, the exploration and advancement of high-efficiency and economically viable solar cells underpin the technological progress for securing energy. Within this domain, conventional crystalline silicon-based solar cells have achieved successful commercialization notwithstanding certain constraints formerly. Additionally, dye-sensitized solar cells, organic photovoltaic devices, quantum dot solar cells, and perovskite solar cells (PSCs) have been extensively investigated and developed to enhance cell performance and efficiency.[1–4] LBPs have been elucidated as a highly promising alternative to silicon-based technology, thanks to their robust light absorption characteristics and superior ambipolar charge transport capabilities. They exhibit a lengthy carrier diffusion length (exceeding 1 mm), an extended charge carrier lifetime (surpassing 100 ns), and a low exciton binding energy (less than 25 meV). Recently, substantial research endeavors have been directed towards the advancements of PSCs, resulting in a notable enhancement of their PCE from a mere 3.8% to an impressive 22.7%.[5–8] While LBPs offer notable advantages of efficiency and cost, significant concerns persist regarding their toxic nature and susceptibility to instability, particularly in humid conditions. These issues demand careful attention and targeted strategies for effective mitigation of the problems.[9–11] Rigorous endeavors for addressing these challenges have been undertaken in the advancement of LBP solar cells.

The focus is to integrate the exceptional optoelectronic characteristics of LBPs with heightened stability and non-toxic attributes. Substitutes, including bivalent tin (Sn^{2+}) and germanium (Ge^{2+}), as well as trivalent bismuth (Bi^{3+}) and antimony (Sb^{3+}), have been examined as potential replacements for lead (Pb^{2+}) in perovskite materials. The primary objective of exploring these alternatives is to uphold the exceptional performance of perovskite materials in optoelectronic devices and catalytic applications, while concurrently diminishing the environmental impact associated with the use of lead.[1212–14] Nevertheless, these alternative materials are deemed suboptimal due to inherent issues related to stability and subpar performance.[15–18] An emerging and promising strategy that we

[a]*Department of Physics, The University of Lahore, 53700, Pakistan. E-mail: iftikharphysicsuet@gmail.com*

[b]*Department of Physics, College of Science, Princess Nourah bint Abdulrahman University, P.O.Box 84428, Riyadh 11671, Saudi Arabia*

[c]*School of Electronic Engineering, Kyonggi University, Suwon, Gyeonggi-do 16227, Republic of Korea. E-mail: choiardor@hanmail.net*

take notice is the substitution of one univalent and one trivalent metal cation for Pb within the crystal structure. This leads to the formation of double perovskites (DP), characterized by a formula of $A_2B^+B^{3+}X_6$. Notably, there is a growing interest in the development of LFHDP, where A = Cs^+; B′ = Ag^+, Na^+, Cu^+; B″ = In^{3+}, Bi^{3+}, Sb^{3+}; X = Cl^-, Br^-, or I^-. The appeal of LFHDP lies in their small carrier effective mass, high stability, and non-toxic nature, rendering them promising alternatives to LBPs.[19–22]

Within the realm of metal halide perovskites, $Cs_2AgBiBr_6$ double perovskite has surfaced as a compelling substitute for toxic and unstable lead halide perovskites in diverse optoelectronic applications including solar cells. This is attributed to its exceptional chemical stability, non-toxic nature, and remarkable optoelectronic properties, including prolonged carrier lifetimes.[23–26] However, the $Cs_2AgBiBr_6$ solar cell encounters challenges related to efficiency, primarily attributed to its wide E_g.[27–29] The process of substitution with impurity ions has been acknowledged as a potent approach for augmenting the optical characteristics of halide perovskites. Indeed, among the array of strategies, substitution stands out for its simplicity and ease of application. Additionally, it offers the advantage of modifying the properties of LFHDP without perturbing their crystal structure.[30–33] The incorporation of Ga ions has been substantiated as a promising dopant, exhibiting noteworthy enhancements in both open circuit voltage (V_{oc}) and fill factor (FF) through the mitigation of recombination, consequently resulting in increased efficiency. Ga substitution has demonstrated the potential to ameliorate charge transport by diminishing surface traps.[34–37] Boudoir *et al*. have doped Ga in $Mg_xZn_{1-x}O$ for photovoltaic devices with its concentration of 0.05 (5%), and they showed that this concentration for Ga is optimal.[38] This specific concentration enhances device performance improving the efficiency of capturing charge carriers. Regarding this consequence, 0.05 Ga concentration has been used in this research.

This study presents a novel exploration focused on the successful incorporation of Ga into $Cs_2AgBiBr_6$, a promising LFHDP material. The synthesized $Cs_2Ag_{0.95}Ga_{0.05}BiBr_6$ underwent comprehensive examinations utilizing XRD, UV-vis spectroscopy, and solar simulator measurements. The crystalline structure and phase purity of the material have been elucidated *via* XRD analysis, leading to insights into the influence of Ga substitution on the perovskite lattice. UV-vis spectroscopy delved into the optical properties, revealing shifts in absorption spectra indicative of modifications in the electronic structure. Additionally, solar simulator measurements assessed the photoconversion efficiency and performance of $Cs_2Ag_{0.95}Ga_{0.05}BiBr_6$, positioning it as a compelling candidate for photovoltaic applications. The synergistic application of these characterization techniques provides a holistic understanding of the structural, optical, and photovoltaic attributes of the pioneering $Cs_2Ag_{0.95}Ga_{0.05}BiBr_6$. This contribution offers invaluable insights to the evolving realm of LFHDPs for sustainable energy technologies. Importantly, this research provides the first comprehensive explanation of the enhanced solar-cell properties caused by $Cs_2Ag_{0.95}Ga_{0.05}BiBr_6$.

2. Experimentation

213 mg of CsBr (with a purity of 99.9% from Sigma-Aldrich), 225 mg of $BiBr_3$ (with a purity of 99.99% from Sigma-Aldrich), and 94 mg of AgBr (with a purity of 99.9% from Alfa Aesar) were introduced into a 25 mL solution of 47% hydrobromic acid (HBr, Alfa Aesar). The resultant mixture underwent stirring at a temperature of 120 °C until the solvent evaporated, yielding red crystals. Stirring was then terminated, and the mixture underwent controlled cooling at a rate of 5 °C per hour. Subsequently, the mixture was allowed to stand undisturbed overnight. The red crystals that precipitated were subsequently subjected to filtration and collection. A subsequent ethanol wash was administered to the collected crystals. The resultant solid product underwent drying under vacuum conditions at 60 °C, culminating in the formation of $Cs_2AgBiBr_6$ crystals. The identical procedure was replicated for Ga substitution, where 5 wt% Ga was incorporated along with all the chemical components.

The phase structure and particle size of both pristine and $Cs_2Ag_{0.95}Ga_{0.05}BiBr_6$ films were investigated using XRD. XRD analysis was performed employing a PANalytical X'Pert PRO MRD X-ray diffractometer equipped with a Ni-filtered Cu Kα source (wavelength = 1.5418 Å). This instrument facilitated high-resolution and lower-resolution measurements on diverse thin film and powder samples. The X-ray diffractometer operated under conditions of 40.0 kV and 40.0 mA. For the optical characterization of the films, a Shimadzu UV-2101 spectrometer was employed.

A total of 532 mg of $Cs_2AgBiBr_6$ and $Cs_2Ag_{0.95}Ga_{0.05}BiBr_6$ powders were dissolved in dimethyl sulfoxide (1 mL, DMSO, 99.9%, Sigma-Aldrich) to prepare 0.5 M precursor solutions for $Cs_2AgBiBr_6$ and $Cs_2Ag_{0.95}Ga_{0.05}BiBr_6$. Subsequently, 100 μL of these solutions underwent spin-coating on the surface of a glass/FTO/TiO_2 layer at 3000 revolutions per minute (rpm) for 1 minute. The resulting two films, $Cs_2AgBiBr_6$ and $Cs_2Ag_{0.95}Ga_{0.05}BiBr_6$, were annealed at 280 °C for 5 minutes to ensure the complete formation of a double perovskite phase. The TiO_2 film was synthesized following the procedures outlined in our previously published paper.[39]

To fabricate the hole transport material (HTM), solution (A) was generated by blending 36 mL of tributylphosphine (TBP) with 22 mL of a stock solution containing 520 mg mL^{-1} of lithium bis-trifluoromethyl sulfonyl-imide. Within solution (A), 72 mg of spiro-OMeTAD was introduced and stirred, resulting in the formation of a solution denoted as solution (B). Subsequently, 1 mL of chlorobenzene was incorporated into solution (B) to create the final solution. For enhanced connectivity of the device with an external source, an 80 nm-thick gold layer was deposited onto the electrode. These solar cells possessed an active area of 0.16 cm^2 and followed the configuration: glass/FTO/TiO_2/$Cs_2AgBiBr_6$/spiro-OMeTAD/Au.[40]

For the evaluation of solar cells, a solar simulator was employed, featuring calibrated air mass (AM) 1.5 G and an intensity of 100 mW cm^{-2}. The testing apparatus was equipped with a computer-controlled source meter, specifically the

Keithley 2400 (manufactured by Keithley Instruments, Inc., Cleveland, OH, USA). This setup was utilized to generate the *J–V* curve, and the voltage sweep was carried out in the reverse bias direction, ranging from 1.2 V to 0 V. The device underwent assessment under standard 1 sun illumination at an air mass (AM) of 1.5 G, and the voltage sweep was executed at a scan rate of 0.2 V s^{-1} (Fig. 1).[41]

3. Results and discussion

3.1. Structure analysis

For characterization, the $Cs_2AgBiBr_6$ film was initially synthesized using the sol–gel method. The crystalline structure was determined through XRD.[42,43] The diffraction peaks for pure $Cs_2AgBiBr_6$ were identified on the (200), (220), (222), (400), (420), and (440) planes, corresponding to 2θ values of 16.56, 22.40, 27.50, 32.30, 36.95, and 38.62, degrees, respectively. The obtained results closely align with the standard JCPDS data for $Cs_2AgBiBr_6$, as indicated by the corresponding file number (01-084-8699). Remarkably, with a 5% Ga substitution, XRD peaks exhibited a shift toward higher 2θ angles, notably evident in the (400) diffraction peak as depicted in Fig. 2(a). Specifically, the peak observed at (400) for the undoped sample at 32.30° shifted to 32.59° with Ga substitution. Upon Ga substitution, no additional peaks were detected, affirming that Ga substitution did not introduce secondary phases or impurities alongside pristine $Cs_2AgBiBr_6$. This confirms Ga substitution in $Cs_2AgBiBr_6$. Also, there was an observed augmentation in peak intensity, indicative of the higher crystallinity by the substitution of Ga ions. The observed peak shifting toward higher angles corresponds to in-plane compressive stress in the film. The introduction of smaller ions into the host lattice results in a peak shifting, attributed to the replacement of Ag^+ by Ga^{3+} due to the disparity in atomic radii between Ag^+ (1.15 Å) and Ga^{3+} (0.62 Å).[44–47] The Scherer equation given below can be utilized to calculate the grain size of the material:[48,49]

$$D = \frac{K\lambda}{\beta\cos\theta} \quad (1)$$

The Scherer constant, denoted as K, is 0.9, and the wavelength (λ) is 1.54 Å. Here, β represents the Full Width at Half Maximum of the peak, and θ denotes the Bragg angle. Therefore, the grain size calculated using eqn (1) is 29 nm for pristine $Cs_2AgBiBr_6$, and is 35 nm for the substitution sample.

The dislocation line density is a metric that quantifies the density of dislocations within a defined volume of a crystalline material. It is defined as $\delta = D^{-2}$ which denotes the length of dislocation lines per unit volume of the crystal and is conventionally expressed in meters per cubic meter (m m^{-3}).[48] The dislocation line density for pristine $Cs_2AgBiBr_6$ was measured at 1.18×10^{-3} m m^{-3}, whereas for the Ga substitution sample, it decreased to 8.16×10^{-4} m m^{-3}. The reduction in dislocation line density has the potential to mitigate the recombination rate, leading to an increase in carrier lifetime. As a result, this enhancement can positively impact the V_{oc}, J_{sc}, and overall PCE of the solar cell.[50–53] Interplanar *d*-spacing (*d*) is a vital parameter in X-ray diffraction analysis, utilized for discerning the crystal structure of a material. The *d*-spacing signifies the perpendicular distance between two successive crystallographic planes of atoms within a crystal lattice. The value of *d* significantly influences the optical and electronic properties of the perovskite, thereby impacting the overall performance of the solar cell.[54] The *d* can be determined using a formula called Bragg's law:[55]

$$d = \lambda/2 \sin\theta \quad (2)$$

where λ is the wavelength and θ is the angle of incidence. The *d* for the pristine sample is 2.76 Å, and for the substitution sample, it is 2.74 Å. The lattice parameter (*a*) is a measurement characterizing the length of the edges of the unit cell, which serves as the smallest repeating structural building block within the crystal. The value of '*a*', especially for the most prominent peak reflection, can be determined through a specific mathematical expression. The volume of the unit cell is directly proportional to the cube of this 'a', as defined by the following mathematical expression.[56]

$$a = d(h^2 + k^2 + l^2)^{1/2} \quad (3)$$

In this context, *d* represents the interplanar spacing, and *h*, *k*, and *l* are the Miller indices. The lattice parameter for the pure sample is 11.07 Å and decreases to 10.98 Å after substitution. The volume a^3 can be easily computed using the relationship in eqn (3). For the pure sample, the volume is 2.22×10^{-8} m^3, and for the substitution sample, it is 2.20×10^{-8} m^3. This reveals discernible differences in the structural properties between the pristine and 5% substitution of Ga into $Cs_2AgBiBr_6$.

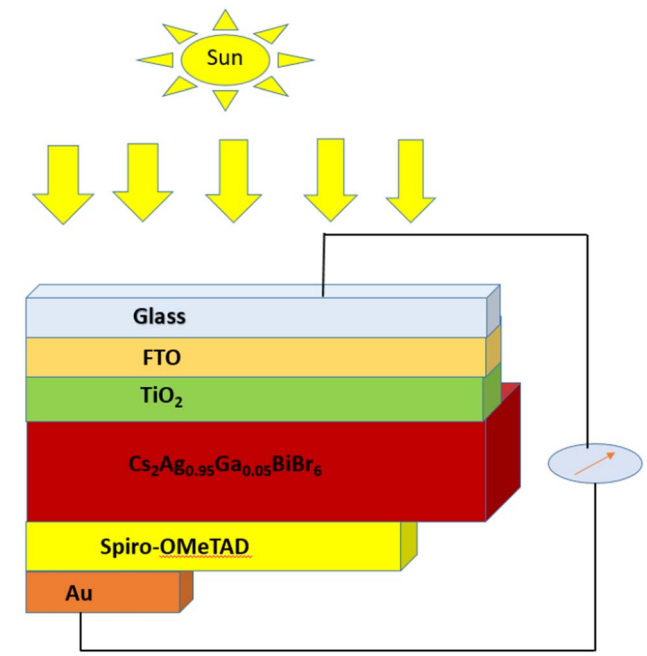

Fig. 1 Geometry of solar cell.

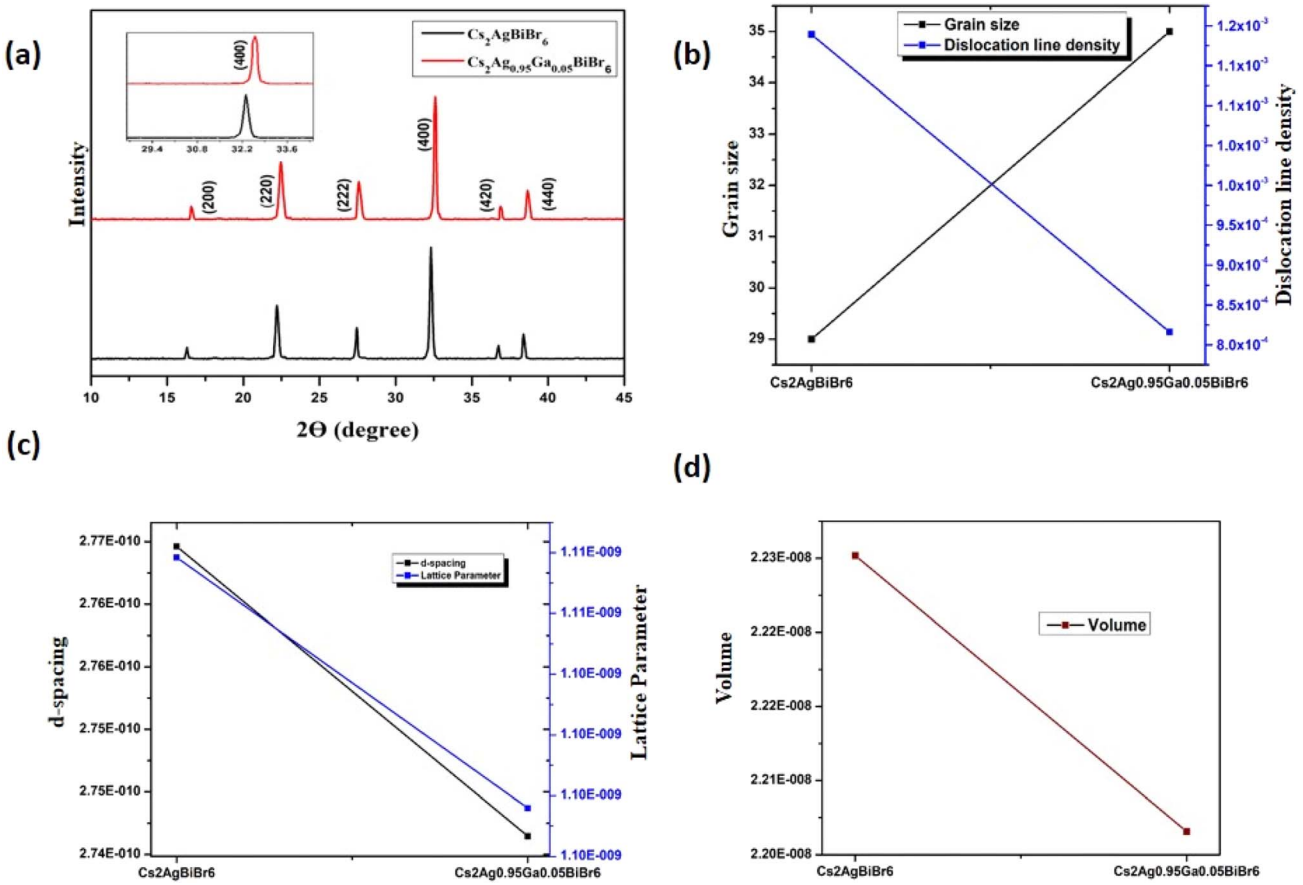

Fig. 2 (a) XRD pattern of pure and $Cs_2Ag_{0.95}Ga_{0.05}BiBr_6$ halide double perovskite solar cell. (b) Crystallite Size and Dislocation Line Density of $Cs_2Ag_{0.95}Ga_{0.05}BiBr_6$. (c) *D*-spacing, lattice parameter of pure and $Cs_2Ag_{0.95}Ga_{0.05}BiBr_6$. (d) Shows the volume for pure and substitution.

Considering effective ionic radii, the Ga^{3+} ion (0.62 Å) exhibits a smaller size than the Ag^{+} ion (1.15 Å). As per Vegard's law, the introduction of Ga through substitution induces structural shrinkage, leading to a reduction in volume.[57]

3.2. Optical analysis

To determine the optical E_g, UV-visible spectroscopy was conducted. The response of the material to light irradiation is significantly influenced by its E_g and the energy conveyed by the incident photons. When photons interact with the material, they impart energy ($h\nu$) to the electrons, elevating electrons' energy so that they occupy higher energy levels beyond the material's E_g. In this process, the excess energy are absorbed by the electrons through interband transitions. This phenomenon is crucial in scrutinizing the absorption edges of a material. The material's E_g can be ascertained by applying Tauc's formula to these absorption edges.[48,58,59]

$$(\alpha h\nu)^2 = B(h\nu - E_g) \quad (4)$$

In this context, α represents the absorption coefficient, B is a constant, $h\nu$ signifies the energy of the incident photon, and E_g denotes the material's bandgap. The value of E_g was determined from Fig. 3(a) by extrapolating it to the zero-ordinate. The optical E_g for pure $Cs_2AgBiBr_6$ was found to be 1.91 eV, and for Ga substitution, the E_g decreased to 1.86 eV. The observed reduction in E_g in the $Cs_2Ag_{0.95}Ga_{0.05}BiBr_6$ film occurred because the Ag 4d-derived valence band (VB) shifted to a higher energy level. This shift was primarily attributed to the overlap between the Ga 4p orbitals and the Ag 4d orbitals.[60] The reduction in E_g could be attributed to an increase in grain size and a decrease in the number of grain boundaries.[61] This is advantageous because a decreased E_g can lead to improved light absorption within the visible spectrum. The bending and propagation of light rays when they transit from one medium to another can be explained by the refractive index (n), which is of the form.[62]

$$n = \sqrt{1 + \left(\frac{A}{E_g + B}\right)} \quad (5)$$

where A and B are constants with values of 13.6 eV and 3.4 eV, the value of n for pristine $Cs_2AgBiBr_6$ is 2.74, and for Ga substitution, it is 2.77. Researchers have indicated that n and E_g are fundamental characteristics of optical materials due to their close connection with the electronic properties of the material. Eqn (5) demonstrates a strong correlation between the n and E_g. Specifically, a reduction in E_g corresponds to an elevation in the n. The increase in n signifies a higher concentration of charge

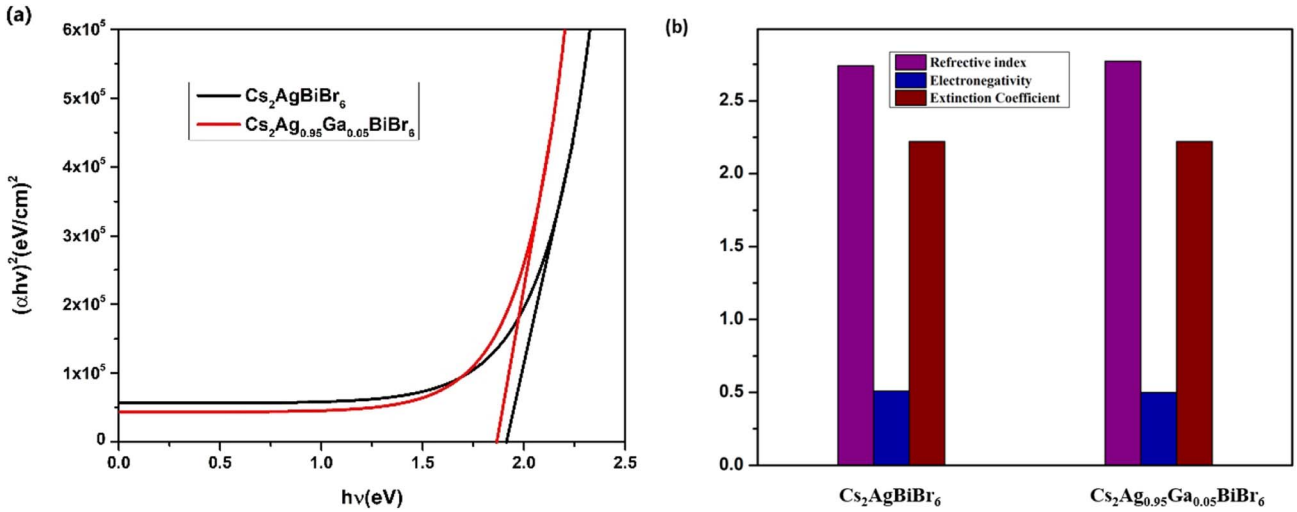

Fig. 3 (a) E_g of pure and $Cs_2Ag_{0.95}Ga_{0.05}BiBr_6$ films. (b) Refractive index, electronegativity, and extinction co-efficient of pure and $Cs_2Ag_{0.95}Ga_{0.05}BiBr_6$.

carriers, leading to a reduction in E_g. This reduction is attributed to an increase in the number of energy states between the conduction and valence bands. Moreover, this increase in 'n' serves as proof of an enlarged presence of polarizable molecules, resulting in a modification of the speed of light within the material.[63]

Electronegativity is defined as the atom's capacity within a molecule to attract electrons to itself. Optical electronegativity provides valuable insights into nature of chemical bonding.[64,65] Optical electronegativity not only offers profound insights into the essence of chemical bonding, but shedding light on the intricate connections that govern molecular structures as well.[66] On the Pauling scale, when the electronegativity difference is below 0.5, it commonly leads to a non-polar covalent bond. The connection between the E_g and optical electronegativity (χ^*) in different binary systems is articulated as follows:[67–69]

$$E_g = 3.72(\Delta\chi^*) \quad (6)$$

where $\Delta\chi^*$ is the difference of the electronegativity between anion and cation. In the case of pristine $Cs_2AgBiBr_6$, the $\Delta\chi^*$ value is 0.51, while for $Cs_2Ag_{0.95}Ga_{0.05}BiBr_6$, it reduces to 0.5. This indicates that as $\Delta\chi^*$ decreases, the E_g also tends to decrease. With an electronegativity difference of only 0.01, this observation implies the existence of a nonpolar covalent bond. The extinction coefficient (k) plays a crucial role in elucidating the dielectric properties of a material. It directly influences emissivity, absorption coefficient, and the total power radiated from a film. This relationship is expressed as $k = n/(\Delta\chi 002a)^{\gamma}$.[55] In this context, the value of γ is -0.32 (a constant). The calculated value of k is 2.220 for pristine $Cs_2AgBiBr_6$ and 2.221 for $Cs_2Ag_{0.95}Ga_{0.05}BiBr_6$. When electromagnetic radiation, such as a light wave, interacts with a material, the complex dielectric function provides valuable insights into the optical behavior of the material.[55,70] The dielectric constant (ε), closely linked to a solid material's polarizability, serves as an indicator of a medium's polarity. In this context, ε is typically represented by its real (ε_r) and imaginary (ε_i) parts as:[71]

$$\varepsilon = \varepsilon_r + i\varepsilon_i \quad (7)$$

ε_r and ε_i which appeared here can be represented as follows:

$$\varepsilon_r = n^2 - k^2 \quad (8)$$

$$\varepsilon_i = 2nk \quad (9)$$

ε_r portrays the degree of materials' polarization when subjected to incident light or an electromagnetic field.[39] ε_i signifies the light absorption in the material.[72] The values of ε_r and ε_i for the undoped material are 2.62 and 12.21, respectively, whereas ε_r is 2.75 and ε_i is 12.31 for the substitution material, as shown in Fig. 4. From this, we see that both ε_r and ε_i increase with substitution. The increase of ε_i indicates enhanced light absorption due to substitution, and this enhancement leads to a greater generation of electron–hole pairs. Consequently, this results in a higher current flow through the circuit, boosting the current density of the solar cell. This, in turn, can contribute to an overall improvement in the efficiency of the solar cell, making it more effective at converting sunlight into electricity.

3.3. *J–V* curve

Fig. 5 illustrates the *J–V* curves for the device fabricated with Ga substitution, and the essential photovoltaic parameters are detailed in Table 1. The $Cs_2AgBiBr_6$ solar cell exhibited a PCE of 3.51%, accompanied by a V_{oc} of 0.92 V, J_{sc} of 5.13 mA cm^{-2}, and FF of 0.73. Substitution with Ga in the LFHDP displayed significantly improved performance. Specifically, the PCE of the cell increased to 4.52%, with elevated values for V_{oc}, J_{sc}, and FF at 0.94 V, 6.01 mA cm^{-2}, and 0.80, respectively.

The J_{sc} signifies the electric current coursing through the external circuit when the solar cell's electrodes are directly

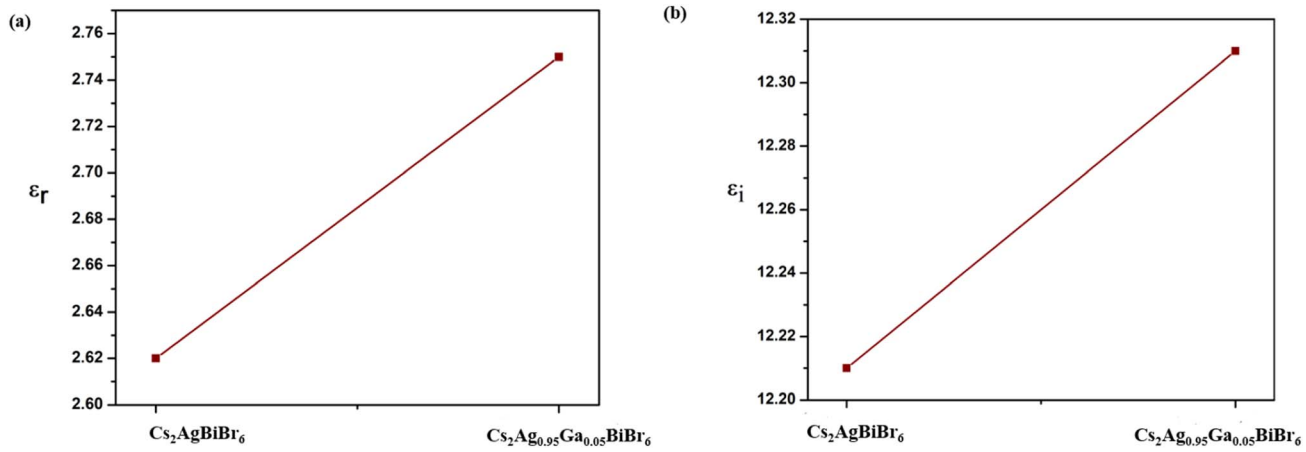

Fig. 4 (a) Shows the real part of ε. (b) Shows the imaginary part of ε for pristine and $Cs_2Ag_{0.95}Ga_{0.05}BiBr_6$.

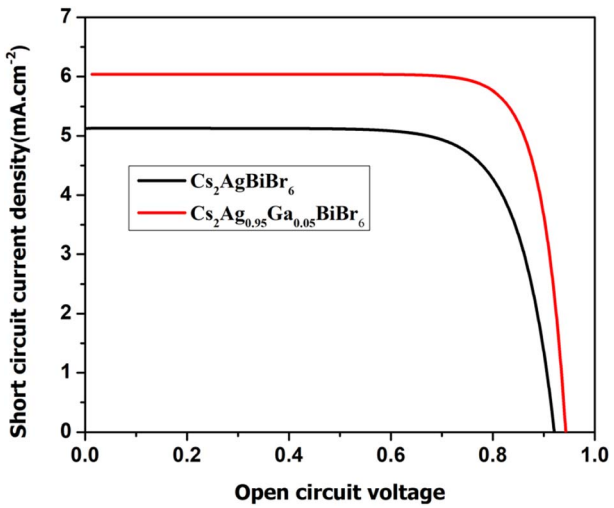

Fig. 5 J–V curve of pure and Ga substitution films.

Table 1 Solar cell parameters of pure and $Cs_2Ag_{0.95}Ga_{0.05}BiBr_6$

Samples	J_{sc} (mA cm^{-2})	V_{oc} (V)	FF	Efficiency η (%)
$Cs_2AgBiBr_6$	5.13	0.92	0.73	3.48
$Cs_2Ag_{0.95}Ga_{0.05}BiBr_6$	6.01	0.94	0.80	4.52

linked. The J_{sc} value of a solar cell is affected by the photon flux produced by the incident light and is dictated by the spectral composition of the light. J_{sc} is a frequently employed term to characterize the maximum current output achievable from a solar cell.[73] The J_{sc} of $Cs_2AgBiBr_6$ for pristine material is 5.13 mA cm^{-2}, and following substitution with Ga, its value increases to 6.01 mA cm^{-2}. An increase in the J_{sc} in a solar cell contributes to improving power output, efficiency, and overall performance of the solar cell.[74] The V_{oc} is the electric potential difference between two terminals of a device when no external load is applied. It represents the maximum voltage achievable from a solar cell and corresponds to the forward bias voltage. Also, it relies on the photo-generated current density. The V_{oc} value for the undoped material is 0.92 V, and after substitution, it increases to 0.94 V.[75,76] It might be possible that Ga substitution in $Cs_2AgBiBr_6$ could increase the carrier concentration and induce an upward shift of the Fermi level of $Cs_2AgBiBr_6$, facilitating the injection and transfer of electrons to the conduction band of perovskite. Simultaneously, by increasing the carrier concentration, the electrons could effectively fill the interface traps, reducing interface trap density. This is beneficial for decreasing electron capture and preventing carrier recombination, eventually improving electron transport efficiency in perovskite. These enhancements could positively impact the photovoltaic properties of the device, such as J_{sc} and V_{oc}.[77–79] The FF is a parameter that characterizes the shape of the current–voltage (J–V) curve of a solar cell. It is the ratio of the maximum power (P_{max}) to the product of the V_{oc} and J_{sc}. Hence, the FF is calculated by the relation.[80]

$$FF = \frac{P_{max}}{J_{sc} \times V_{oc}} \quad (10)$$

The FF value for the undoped sample is 0.73, and after substitution, its value increases to 0.80. The increase in FF value indicates that the solar cell is more efficient in converting sunlight into electricity.

The PCE of a solar cell is a measure of how well it converts sunlight into electricity. It is defined as the ratio of the maximum power output (P_{max}) to the incident solar power. Accordingly, the mathematical expression for PCE is of the form[81]

$$\eta = \frac{V_{oc} \times J_{sc} \times FF}{P_{in}} \quad (11)$$

The PCE of the LFHDP is 3.48% for the pristine specimen, and with substitution, the value escalates to 4.52%. This increase in PCE is ascribed to the elevation of the values J_{sc}, V_{oc}, and FF, resulting from the substitution. The enhanced J–V

parameters observed in cells with an optimal content of $Cs_2Ag_{0.95}Ga_{0.05}BiBr_6$ can be attributed to higher electrical conductivity and an upward shift of the Fermi level. Therefore, the improved photovoltaic results suggest a reduction in charge carrier recombination at $Cs_2AgBiBr_6$.

4. Conclusion

In conclusion, this research demonstrates the strong points of $Cs_2Ag_{0.95}Ga_{0.05}BiBr_6$ in relation with enhancing the performance of the device. $Cs_2AgBiBr_6$ films were successfully synthesized using the sol–gel method, as confirmed by XRD analysis. The $Cs_2Ag_{0.95}Ga_{0.05}BiBr_6$ revealed peak shifts towards higher angles, indicative of achieving Ga substitution. Then, we focused on exploring the impact of the presence of Ga on the structural, optical, and dielectric properties of $Cs_2AgBiBr_6$. The introduction of Ga led to larger grain sizes in the $Cs_2AgBiBr_6$ films. Optical properties, including E_g, electronegativity, k, and ε, were determined using UV-Vis spectroscopy. With 5% Ga substitution, the solar cell exhibited improved parameters: $J_{sc} = 6.01$ mA cm^{-2}, $V_{oc} = 0.94$ V, FF = 0.80, and PCE = 4.52%. This research not only successfully addresses challenges in film formation but also provides constructive insights into the potential of $Cs_2Ag_{0.95}Ga_{0.05}BiBr_6$ as a high-performance and stable material for photovoltaic applications. The findings contribute to the technology of developing environmentally friendly and efficient solar cells, paving the way for the future adoption of lead-free perovskites in the solar energy landscape.

Conflicts of interest

The authors have no conflict of interest.

Acknowledgements

This research was supported by Princess Nourah bint Abdulrahman University Researchers Supporting Project number (PNURSP2024R327), Princess Nourah bint Abdulrahman University, Riyadh, Saudi Arabia. This work was supported by the National Research Foundation of Korea (NRF) grant funded by the Korea government (MSIT) (No. NRF-2021R1F1A1062849).

References

1 F. Liu, Q. Li and Z. Li, Hole-transporting materials for perovskite solar cells, *Asian J. Org. Chem.*, 2018, 7(11), 2182–2200.
2 S. Tabrizian, Technological innovation to achieve sustainable development—Renewable energy technologies diffusion in developing countries, *Sustainable Dev.*, 2019, **27**(3), 537–544.
3 S. Almosni, *et al.*, Material challenges for solar cells in the twenty-first century: directions in emerging technologies, *Sci. Technol. Adv. Mater.*, 2018, **19**(1), 336–369.
4 T. T. Vu, *An Investigation into Current Challenges in Solar Cell Technology*, 2021.
5 C.-H. Chiang, M. K. Nazeeruddin, M. Grätzel and C.-G. Wu, The synergistic effect of H 2 O and DMF towards stable and 20% efficiency inverted perovskite solar cells, *Energy Environ. Sci.*, 2017, **10**(3), 808–817.
6 H. Lei, D. Hardy and F. Gao, Lead-free double perovskite Cs2AgBiBr6: fundamentals, applications, and perspectives, *Adv. Funct. Mater.*, 2021, **31**(49), 2105898.
7 S. Bhaumik, S. Ray and S. K. Batabyal, Recent advances of lead-free metal halide perovskite single crystals and nanocrystals: synthesis, crystal structure, optical properties, and their diverse applications, *Mater. Today Chem.*, 2020, **18**, 100363.
8 L. Zhang, *et al.*, Advances in the application of perovskite materials, *Nano-Micro Lett.*, 2023, **15**(1), 177.
9 P. Mahajan, *et al.*, Recent progress, fabrication challenges and stability issues of lead-free tin-based perovskite thin films in the field of photovoltaics, *Coord. Chem. Rev.*, 2021, **429**, 213633.
10 X. Li, *et al.*, Dimensional Diversity (0D, 1D, 2D, 3D) in Perovskite Solar Cells: Exploring the Potential of Mix-dimensional Integrations, *J. Mater. Chem. A*, 2024, 1–7.
11 X. Zhu, *et al.*, Fabrication of high-performance silver mesh for transparent glass heaters *via* electric-field-driven microscale 3D printing and UV-assisted microtransfer, *Adv. Mater.*, 2019, **31**(32), 1902479.
12 Z. Wu, *et al.*, Recent developments in lead-free bismuth-based halide perovskite nanomaterials for heterogeneous photocatalysis under visible light, *Nanoscale*, 2023, **15**, 5598–5622.
13 H. Li, *et al.*, 3D printed high performance silver mesh for transparent glass heaters through liquid sacrificial substrate electric-field-driven jet, *Small*, 2022, **18**(17), 2107811.
14 H. Zhang, *et al.*, Recent advances in nanofiber-based flexible transparent electrodes, *Int. J. Extreme Manuf.*, 2023, **5**, 3–8.
15 E. L. Lim, A. Hagfeldt and D. Bi, Toward highly efficient and stable Sn 2+ and mixed Pb 2+/Sn 2+ based halide perovskite solar cells through device engineering, *Energy Environ. Sci.*, 2021, **14**(6), 3256–3300.
16 N. K. Noel, *et al.*, Lead-free organic–inorganic tin halide perovskites for photovoltaic applications, *Energy Environ. Sci.*, 2014, **7**(9), 3061–3068.
17 M. Wang, *et al.*, Reversible calcium alloying enables a practical room-temperature rechargeable calcium-ion battery with a high discharge voltage, *Nat. Chem.*, 2018, **10**(6), 667–672.
18 S. Li, *et al.*, Comparative study of the micro-mechanism of charge redistribution at metal-semiconductor and semimetal-semiconductor interfaces: Pt (Ni)-MoS2 and Bi-MoS2 (WSe2) as the prototype, *Appl. Surf. Sci.*, 2023, **623**, 157036.
19 F. Giustino and H. J. Snaith, Toward lead-free perovskite solar cells, *ACS Energy Lett.*, 2016, **1**(6), 1233–1240.
20 J. Luo, *et al.*, Efficient and stable emission of warm-white light from lead-free halide double perovskites, *Nature*, 2018, **563**(7732), 541–545.

21 X. Zhang, Y. Tang, F. Zhang and C. S. Lee, A novel aluminum–graphite dual-ion battery, *Adv. Energy Mater.*, 2016, **6**(11), 1502588.
22 C. Lu, *et al.*, BaCo0. 4Fe0. 4Nb0. 1Sc0. 1O3-δ perovskite oxide with super hydration capacity for a high-activity proton ceramic electrolytic cell oxygen electrode, *Chem. Eng. J.*, 2023, **472**, 144878.
23 R. L. Hoye, *et al.*, Fundamental carrier lifetime exceeding 1 μs in Cs2AgBiBr6 double perovskite, *Adv. Mater. Interfaces*, 2018, **5**(15), 1800464.
24 J. A. Steele, *et al.*, Photophysical pathways in highly sensitive Cs2AgBiBr6 double-perovskite single-crystal X-ray detectors, *Adv. Mater.*, 2018, **30**(46), 1804450.
25 Y. Wu, *et al.*, Metastable structures with composition fluctuation in cuprate superconducting films grown by transient liquid-phase assisted ultra-fast heteroepitaxy, *Mater. Today Nano*, 2023, **24**, 100429.
26 X. Yang, *et al.*, Transformation of waste battery cathode material LiMn2O4 into efficient ultra-low temperature NH3-SCR catalyst: Proton exchange synergistic vanadium modification, *J. Hazard. Mater.*, 2023, **459**, 132209.
27 S. Zhao, *et al.*, First-principles study of electronic and optical properties of lead-free double perovskites Cs2NaBX6 (B= Sb, Bi; X= Cl, Br, I), *J. Phys. Chem. Solids*, 2018, **117**, 117–121.
28 P. Sebastia-Luna, *et al.*, Tuning the Optical Absorption of Sn-, Ge-, and Zn-Substituted Cs2AgBiBr6 Double Perovskites: Structural and Electronic Effects, *Chem. Mater.*, 2021, **33**(20), 8028–8035.
29 C.-H. Li, *et al.*, Excellent-moisture-resistance fluorinated polyimide composite film and self-powered acoustic sensing, *ACS Appl. Mater. Interfaces*, 2023, **15**(29), 35459–35468.
30 Y. Zhou, J. Chen, O. M. Bakr and H.-T. Sun, Metal-doped lead halide perovskites: synthesis, properties, and optoelectronic applications, *Chem. Mater.*, 2018, **30**(19), 6589–6613.
31 S. Das Adhikari, R. K. Behera, S. Bera and N. Pradhan, Presence of metal chloride for minimizing the halide deficiency and maximizing the doping efficiency in Mn (II)-doped CsPbCl3 nanocrystals, *J. Phys. Chem. Lett.*, 2019, **10**(7), 1530–1536.
32 J. Yin, *et al.*, Unlocking the effect of trivalent metal doping in all-inorganic CsPbBr3 perovskite, *ACS Energy Lett.*, 2019, **4**(3), 789–795.
33 S. Mu, *et al.*, Molecular grafting towards high-fraction active nanodots implanted in N-doped carbon for sodium dual-ion batteries, *Natl. Sci. Rev.*, 2021, **8**(7), nwaa178.
34 Z. Ma, *et al.*, Negligible hysteresis planar perovskite solar cells using Ga-doped SnO2 nanocrystal as electron transport layers, *Org. Electron.*, 2019, **71**, 98–105.
35 S. S. Mali, J. V. Patil, H. Kim and C. K. Hong, Gallium cationic incorporated compact TiO2 as an efficient electron-transporting layer for stable perovskite solar cells, *Matter*, 2019, **1**(2), 452–464.
36 S. G. Shin, I. T. Kim and H. W. Choi, A study of perovskite solar cell with a Fe3+/Ga3+ doped TiO2 layer, *Jpn. J. Appl. Phys.*, 2020, **59**(SG), SGGF05.
37 D. Wang, *et al.*, Molecular level manipulation of charge density for solid-liquid TENG system by proton irradiation, *Nano Energy*, 2022, **103**, 107819.
38 S. Boudour, I. Bouchama, and M. Hadjab. Optimization of CdTe solar cell performances using Ga-doped MgxZn1-xO buffer layer, in *6th International Symposium on Transparent Conductive Materials*, 2016.
39 M. Khan, *et al.*, Structural, electrical and optical properties of multilayer TiO2 thin films deposited by sol–gel spin coating, *Results Phys.*, 2017, **7**, 1437–1439.
40 S. Hussain, *et al.*, The effect of 600 keV Ag ion irradiation on the structural, optical, and photovoltaic properties of MAPbBr3 films for perovskite solar cell applications, *Materials*, 2022, **15**(15), 5299.
41 M. I. Khan, *et al.*, Bi and Sn Doping Improved the Structural, Optical and Photovoltaic Properties of MAPbI3-Based Perovskite Solar Cells, *Materials*, 2022, **15**(15), 5216.
42 Z. Huang, P. Luo, Q. Wu and H. Zheng, Constructing one-dimensional mesoporous carbon nanofibers loaded with NaTi2 (PO4) 3 nanodots as novel anodes for sodium energy storage, *J. Phys. Chem. Solids*, 2022, **161**, 110479.
43 K. Wang, *et al.*, Air plasma-sprayed high-entropy (Y0. 2Yb0. 2Lu0. 2Eu0. 2Er0. 2) 3Al5O12 coating with high thermal protection performance, *J. Adv. Ceram.*, 2022, **11**(10), 1571–1582.
44 S. Erkan, *et al.*, Enhanced photovoltaic performance of silicon-based solar cell through optimization of Ga-doped ZnO layer, *Phys. Scr.*, 2023, **98**(10), 105928.
45 K. Shtereva, *et al.*, Effect of annealing on properties of sputtered and nitrogen-implanted ZnO: Ga thin films, *EPJ Photovoltaics*, 2012, **3**, 35003.
46 H. Peng, *et al.*, Simultaneous realization of broad temperature stability range and outstanding dielectric performance in (Ag+, Ta5+) co–doped TiO2 ceramics, *J. Alloys Compd.*, 2019, **783**, 423–427.
47 Y. Zhang, X. Liu, M. Song and Z. Qin, Tuning the Red-to-Green-Upconversion Luminescence Intensity Ratio of Na3ScF6: 20% Yb3+, 2% Er3+ Particles by Changes in Size, *Materials*, 2023, **16**(6), 2247.
48 M. Amjad, *et al.*, Photovoltaic properties of ZnO films Co-doped with Mn and La to enhance solar cell efficiency, *Nanomaterials*, 2022, **12**(7), 1057.
49 M. Khan, *et al.*, 900 keV Au ions implantation effect on the efficiency of dye sensitized solar cells, *Results Phys.*, 2019, **14**, 102425.
50 I. Sabid, S. Hasan, R. Islam, and I. M. Mehedi, Effect of dislocation density on the performance of InGaN-based MJ solar cell: Analytical approach, in *2015 2nd International Conference on Electrical Information and Communication Technologies (EICT)*, IEEE, 2015.
51 K. N. Yaung, M. Vaisman, J. Lang and M. L. Lee, GaAsP solar cells on GaP/Si with low threading dislocation density, *Appl. Phys. Lett.*, 2016, **109**(3), 032107.
52 L. Lu, *et al.*, Study on current discrepancy and redistribution of HTS non-insulation closed-loop coils during charging/discharging and subsequent transient process toward

steady-state operation, *Supercond. Sci. Technol.*, 2022, **35**(9), 095001.

53 Z. Yan, *et al.*, Mechanism and technology evaluation of a novel alternating-arc-based directed energy deposition method through polarity-switching self-adaptive shunt, *Addit. Manuf.*, 2023, **67**, 103504.

54 F. Peña-Camargo, *et al.*, Revealing the doping density in perovskite solar cells and its impact on device performance, *Applied Physics Reviews*, 2022, **9**(2), 021409.

55 M. I. Khan, *et al.*, Improving the structural, optical and photovoltaic properties of Sb-and Bi-Co-doped MAPbBr3 perovskite solar cell, *Coatings*, 2022, **12**(3), 386.

56 M. Saini, S. Singh, R. Shukla and A. Kumar, Mg doped copper ferrite with polyaniline matrix core–shell ternary nanocomposite for electromagnetic interference shielding, *J. Inorg. Organomet. Polym. Mater.*, 2018, **28**, 2306–2315.

57 A. Sen, *et al.*, Influence of Ba and Mo co-doping on the structural, electrical, magnetic and optical properties of BiFeO3 ceramics, *Mater. Res. Express*, 2020, **7**(1), 016312.

58 M. Khan, *et al.*, Structural, electrical and optical properties of hetrostructured MoS2/ZnO thin films for potential perovskite solar cells application, *J. Mater. Res. Technol.*, 2022, **20**, 1616–1623.

59 S. Yang, *et al.*, Proportional optimization model of multiscale spherical BN for enhancing thermal conductivity, *ACS Appl. Electron. Mater.*, 2022, **4**(9), 4659–4667.

60 K. Kim, H. Kim and J. Park, Bandgap modulation of Cs2AgInX6 (X= Cl and Br) double perovskite nano-and microcrystals *via* Cu2+ doping, *ACS Omega*, 2021, **6**(41), 26952–26958.

61 P. Jain and P. Arun, Influence of grain size on the band-gap of annealed SnS thin films, *Thin Solid Films*, 2013, **548**, 241–246.

62 A. Attia, *et al.*, Tuning the band gap edges of perovskite material by Cd doping for achieving high current density in perovskite solar cells, *Ceram. Int.*, 2023, **49**(12), 20465–20469.

63 S. B. Aziz, Modifying poly (vinyl alcohol)(PVA) from insulator to small-bandgap polymer: A novel approach for organic solar cells and optoelectronic devices, *J. Electron. Mater.*, 2016, **45**(1), 736–745.

64 R. Reddy, *et al.*, Optical electronegativity, bulk modulus and electronic polarizability of materials, *Opt. Mater.*, 2000, **14**(4), 355–358.

65 S. S. Batsanov, Energy Electronegativity and Chemical Bonding, *Molecules*, 2022, **27**(23), 8215.

66 Q.-M. Huang, *et al.*, Ba2 [MoO3 (OH)(IO3) 2] IO3: a promising SHG material featuring a Λ-shaped functional motif achieved by universal mono-site substitution, *Chem. Mater.*, 2020, **32**(15), 6780–6787.

67 R. Reddy, *et al.*, Correlation between optical electronegativity and refractive index of ternary chalcopyrites, semiconductors, insulators, oxides and alkali halides, *Opt. Mater.*, 2008, **31**(2), 209–212.

68 A. Jeelani, S. Muthu, P. Ramesh and A. Irfan, Experimental spectroscopic, molecular structure, electronic solvation, biological prediction and topological analysis of 2, 4, 6-tri (propan-2-yl) benzenesulfonyl chloride: An antidepressant agent, *J. Mol. Liq.*, 2022, **358**, 119166.

69 A. Bahadur and M. Mishra, Correlation Between Refractive Index and Electronegativity Difference for A^NB^8-N Type Binary Semiconductors, *Acta Phys. Pol., A*, 2013, **123**(4), 737–740.

70 Q. Li, *et al.*, Engineering an Ultrathin and Hydrophobic Composite Zinc Anode with 24 μm Thickness for High-Performance Zn Batteries, *Adv. Funct. Mater.*, 2023, 2303466.

71 F. A. Najar, *et al.*, Comparative study of optical properties of substitutionally doped La2NiMnO6 double perovskite ceramic: A potential candidate for solar cells and dielectrics, *Phys. B*, 2021, **621**, 413311.

72 Q. Mahmood, *et al.*, Study of lead-free double perovskites X2AgBiI6 (X= K, Rb, Cs) for solar cells and thermoelectric applications, *J. Mater. Res. Technol.*, 2023, **22**, 913–922.

73 M. Wright and A. Uddin, Organic—inorganic hybrid solar cells: A comparative review, *Sol. Energy Mater. Sol. Cells*, 2012, **107**, 87–111.

74 W. Gao, *et al.*, Simultaneously increasing open-circuit voltage and short-circuit current to minimize the energy loss in organic solar cells *via* designing asymmetrical non-fullerene acceptor, *J. Mater. Chem. A*, 2019, **7**(18), 11053–11061.

75 E. M. A. E. Halium, H. Mansour, N. F. Alrasheedi and A. F. Al-Hossainy, High-performance one and two-dimensional doped polypyrrole nanostructure for polymer solar cells applications, *J. Mater. Sci.: Mater. Electron.*, 2022, **33**(13), 10165–10182.

76 B. Zheng, *et al.*, Turbulent skin-friction drag reduction by annular dielectric barrier discharge plasma actuator, *Phys. Fluids*, 2023, **35**(12), 13–19.

77 Y. Chen, *et al.*, Natively textured surface of Ga-doped ZnO films electron transporting layer for perovskite solar cells: further performance analysis from device simulation, *J. Mater. Sci.: Mater. Electron.*, 2019, **30**, 4726–4736.

78 B. Roose, *et al.*, A Ga-doped SnO 2 mesoporous contact for UV stable highly efficient perovskite solar cells, *J. Mater. Chem. A*, 2018, **6**(4), 1850–1857.

79 Z. Huang, *et al.*, A sulfur-doped carbon-enhanced Na3V2 (PO4) 3 nanocomposite for sodium-ion storage, *J. Phys. Chem. Solids*, 2022, **167**, 110746.

80 S. Bano, *et al.*, Effect of Cd doping on the structural, optical, and photovoltaic properties of SnS films, *J. Mater. Res. Technol.*, 2022, **19**, 1982–1992.

81 M. Khan, *et al.*, Effect of silver (Ag) ions irradiation on the structural, optical and photovoltaic properties of Mn doped TiO2 thin films based dye sensitized solar cells, *Ceram. Int.*, 2021, **47**(11), 15801–15806.